International Journal of Multiphysics
Volume 17, No. 4, 2023
ISSN: 1750-9548

Numerical Investigation of Flow Modification Cooling Technique to Mitigate Aerodynamic Heating and Wave Drag in Hypersonic Flows of 60^0 Blunted Cones

Shyam Singh Kanwar[1], Gajendra Kumar Agrawal[2], Roopesh Kumar Sinha[3], Dinesh Sen[4], Rahul Gupta[5], Bharti Sharma[6], Sharda Pratap Shrivas[7]

[1,2]Department of Mechanical Engineering, Government Engineering College, Bilaspur, C.G., 495009, India

[3]Department of Mechanical Engineering, NMDC DAV Polytechnic, Geedam, Dantewada, C.G., 494441, India

[4]Department of Civil Engineering, Vishwavidyalaya Engineering College, Ambikapur, C.G., 497001, India

[5]Department of Electronics & Telecommunication Engineering, Government Engineering College, Bilaspur, C.G., 495009, India

[6]Department of Civil Engineering, Vishwavidyalaya Engineering College, Ambikapur, C.G., 497001, India

[7]Department of Mechanical Engineering, Chouksey Engineering College Bilaspur, Bilaspur, C.G., India

Corresponding Author Email: shyamkanwar@gecbsp.ac.in

ABSTRACT

This study numerically investigated the effectiveness of an aero-spike in reducing aerodynamic wave drag in hypersonic flow. The research involved numerical simulations using ANSYS Fluent, utilizing the Reynolds-Averaged Navier-Stokes (RANS) equations as the governing equations along with the shear stress transport (SST) k-ω turbulence model. For this study, a 60-degree axisymmetric blunted body was used to attach the aero spike to the nose region. Four different spike tip shapes and lengths were investigated, covering various length-to-base diameter ratios (L/D) of 0.2, 0.5, 0.7, 1, and 1.5. The airflow was maintained at Mach 8.0 with an angle of attack of 0 degrees. The simulation results were compared with theoretical findings, and a favorable agreement was observed. The results highlighted that the performance of the thermal protection system, facilitated by the aero-spike, was notably influenced by the L/D ratio of the spike. The simulation outcomes included surface pressure distributions and temperature profiles for each spike configuration. It was evident that employing different spike types resulted in a significant reduction in pressure drag. The simulations demonstrated that the choice of spike length and shape, determined by the L/D ratio, played a vital role in enhancing the thermal protection system's performance. The results clearly indicated a substantial decrease in pressure drag when employing different types of spikes.

Keywords: Hypervelocity, Mechanical aero-spike, Wave drag mitigation, Aerodynamic wave drag, Flow separation, Recirculation zone

1. INTRODUCTION

Hypersonic vehicles experience significant heating challenges during atmospheric flight, leading to the adoption of large-angle blunt-cone configurations. However, this choice results in increased aerodynamic drag due to the presence of a nearly normal standing shock wave in front of the vehicle. Managing aerodynamic drag is critical for reducing space travel costs and improving the range of supersonic missiles. Various techniques have been proposed to mitigate wave drag by controlling the flow fields around high-speed bodies. These techniques include using aero-spikes with different designs, injecting gas at the stagnation region, and introducing energy into the flow. Recent interest has focused on employing forward-facing mechanical spikes attached at the blunt body's stagnation point to reduce wave drag and heat flux during hypersonic flight. Previous studies by Snezana and Pavlovic (2002), Tahani et al. (2013), and Mansour and Khorsandi (2014) have investigated wave drag reduction and thermal load through numerical analysis and experiments involving forward-facing aero-spikes. This research aims to numerically examine drag reduction achieved by an aero-spike in a 60° apex angle large blunt cone within hypersonic flow using computational fluid dynamics (CFD). The ANSYS software is utilized for the numerical simulation, calculating the flow field around the body at a free stream Mach number of 8.0. To compute drag coefficients, we consider the pressure drag normal to the surface, assuming flow over a perpendicular blunt body with wall shear stress not contributing to drag force. The study proposes the use of an aero-spike as an approach for a fully reusable thermal protection system. This method is expected to yield similar drag reduction at the nose region compared to the mechanical spike approach. The aero-spike functions as an aerodynamic device, displacing the detached shock wave from the nose and creating a recirculation region. This configuration demonstrates high effectiveness in reducing aerodynamic drag at the nose region. Figure 1 provides a schematic diagram illustrating the supersonic flow fields with an aero-spike at the blunt body's nose.

Retractable Aero-spike

The use of a drag-reducing aero-spike in space vehicles aims to minimize aerodynamic drag for blunt bodies during supersonic and hypersonic speeds. By creating a significant shock stand-off distance ahead of the body, the aero-spike contributes to this reduction. A high-strength metal frame is applied to the stagnation point of the nose, resulting in the conversion of a strong bow shock into a weak conical shock or a strong bow shock at the tip of the spike. This configuration creates a recirculation region in front of the body, as shown in Figure 1. The aero-spike can also be retracted to meet specific aerodynamic requirements. However, there are limitations to the effectiveness of the aero-spike technique. The hypersonic motion generates substantial heat in front of the spacecraft or missile, and the spike tip is particularly vulnerable to this heat. Consequently, the spike is susceptible to failure due to the concentrated heat. Researchers have found that this technique is mostly ineffective due to these challenges.

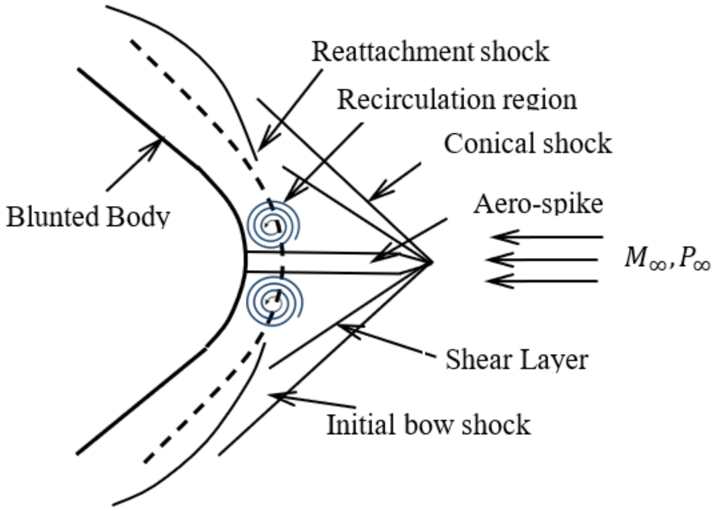

Fig.1 Flow field features around a blunt body with a sharp-tipped spike

2. LITERATURE REVIEW

Numerous researchers worldwide have conducted extensive investigations into mechanical drag reduction using mechanical spikes. These studies have encompassed numerical simulations, experimental tests, and theoretical analyses, focusing on various factors such as spike length-to-base diameter (L/D) ratio, spike tip shape, free stream angle of attack, temperature effects, and force measurements on blunt bodies. For instance, Crawford (1959) performed experimental research to explore the influence of spikes with different L/D ratios on flow fields surrounding hemisphere-cylinders at Mach 6.8. The findings indicated that increasing the spike length reduced drag up to a maximum L/D ratio, beyond which the drag coefficient increased. Additionally, the experiment revealed variations in heat transfer rates, with lower rates observed at low Reynolds numbers. Wood (1962) conducted experimental investigations and observed that the flow near the point of reattachment on the blunt body significantly affected the size and physical shape of the separated flow region. Ahmed and Qin (2011) focused on studying the behavior of a hemispherical body with a spike traveling at hypersonic speeds. They utilized a splitting streamline method to shift the separation point, gaining insights into the mechanism of drag reduction. Bogdonoff and Vas (1959) examined unsteady flow field features and emphasized the drag reduction achieved by employing a spike, highlighting the importance of understanding the spike's size and shape due to the potential development of a recirculation zone and flow instability. Mehta (2012) conducted a numerical study to investigate pressure drag and heat flux reduction using a physical spike with an L/D ratio of 0.5 at Mach 6 and zero angle of incidence. The research revealed that a hemispherical disc spike resulted in significantly higher drag compared to a flat-faced disc spike. Huang et al. (2018) discussed the advantages of employing blunt-shaped structures in various applications such as long-range missiles, spacecraft, and reusable launchers, highlighting the reduced strain on the thermal management system. Kharati and Gazor (2017) utilized computational fluid dynamics (CFD) simulations with the ANSYS solver to explore the effects of spike size and shape on drag reduction. Their findings demonstrated that both factors influenced the drag magnitude. Gauer and Paull (2008) emphasized the need for further research on high-enthalpy flows with spiking topologies, particularly focusing on understanding the impact of gas non-equilibrium flow on wave drag and skin friction drag. Myshenkov (1982) utilized a finite-difference method to solve the complete system of Navier-Stokes equations in a 2D axisymmetric computational domain, observing substantial drag reduction with mechanical spikes in high-speed flows. Paskonov and Cheraneva (1998) solved the unsteady Navier-Stokes equations in a 2D axisymmetric flow field around cone and flat cylinder bodies, incorporating pointed mechanical aero-spikes with different L/D ratios. Huang et al. (2019) mentioned that utilizing aerospike and counter-jet together, generates a complex flow field. To understand this phenomenon in detail, require 3D simulation. Moreover, three-dimensional (3D) effects do not change the flow field patterns. However, 3D effect influence the flow field in areas where the fluid velocity is relatively lower, particularly in subsonic regions within a diffuser and in separation regions caused by the interaction between shock waves and the boundary layer. Gerdroodbary and Hosseinalipour (2010) performed 2D axisymmetric simulations using hemispherical aero-disks under turbulent flow conditions, revealing a decrease in total heat transfer rate. 2D axisymmetric simulations are capable of accurately predicting the flow field and surface properties under hypersonic flow conditions. Lee et al. (2011) their research findings indicated that the steady-state results from the 2D and axisymmetric simulations matched well with experimental data. However, when it came to unsteady simulations, they observed discrepancies in the frequencies of certain unsteady phenomena, with a deviation of approximately 16% compared to the experimental values. Patil et al. (2022) investigated the influence of various flow parameters on surface pressure distribution, surface heat flux, and drag force for hypersonic flow over a hemisphere using in-house designed solvers capable of handling ideal gas and non-equilibrium N-S flow. The findings indicated a reduction in drag coefficient with increasing free stream total enthalpy. Kumar and Kulkarni (2020) conducted numerical analyses to assess the combined effect of mechanical aero-spikes and forward-facing counter jets on hypersonic flows. They used 2D N-S in-house solver for the computation.

3. NUMERICAL METHODOLOGY

3.1 Computational Geometry

In this study, two grid configurations are utilized to analyze the flow fields around a 60° apex-angle blunt body model. All simulations have been conducted in 2D. Figure 2 represents the geometry for the blunt body without a nose spike, while Figure 4 illustrates the geometry configuration with a spike. The blunt body has a diameter of 70 mm and a bluntness ratio of 0.857. The geometry of the blunt body is sourced from various references. The first part of the geometry, corresponding to the blunt body, is based on the work of Kulkarni and Reddy (2021), as well as experimental models used by John et al. (2021) and Venukumar et al. (2006, 2007). The second part of the geometry, representing the spike, is obtained from references such as Menezes et al.

(2003) and Gerdroodbary and Hosseinalipour (2010). The sizes and geometries of different spike types employed in the experimental tests are depicted in Figure 4. To optimize computational efficiency, an axisymmetric simulation approach is employed for the blunt cone geometry, leveraging the assumption of flow symmetry. This allows for simulating only half of the geometry instead of a full 3D model, resulting in significant computational time savings. However, for simulations involving a spherical-shaped spike, a full-scale planar model is used, as shown in Figure 4. The present paper has employed four spike shapes, in which three geometries utilize axisymmetry models, and only a full planar model is used for the hemisphere shape spike. The spike body is cylindrical with a diameter of 2 mm for all geometries. The spike length has been determined according to the L/D ratio for all spike shapes. A cone with a diameter of 70 mm has been used for the spike length in all spike shapes. The cone has been blunted with a radius of 30 The lengths used with this base diameter are 15 mm, 35 mm, 45 mm, 70 mm, and 105 mm, with corresponding ratios of 0.2, 0.5, 0.7, 1, and 1.5 respectively.

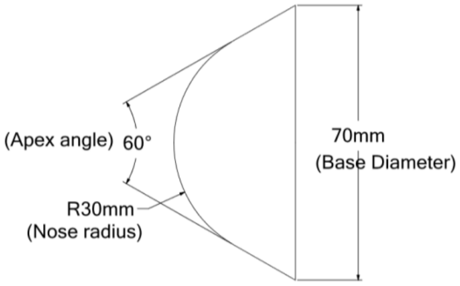

Fig.2 Dimension of 2D blunted cone

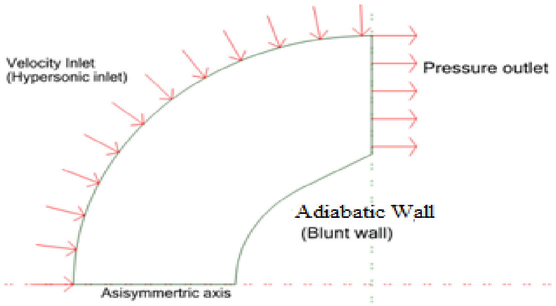

Fig.3 Computational Domain without spike and boundary conditions

For the simulation without a spike condition, the boundary conditions depicted in Figure 3 are utilized. These boundary conditions, set in ANSYS Fluent, include: Inlet boundary condition: Mach 8 at inlet, Outlet boundary condition: Pressure outlet, Wall boundary condition: Adiabatic Wall, Axisymmetric condition: Axis, For the simulation of the retracted aero-spike case, the identical geometry will be employed, originating from the stagnation point of the blunt body.

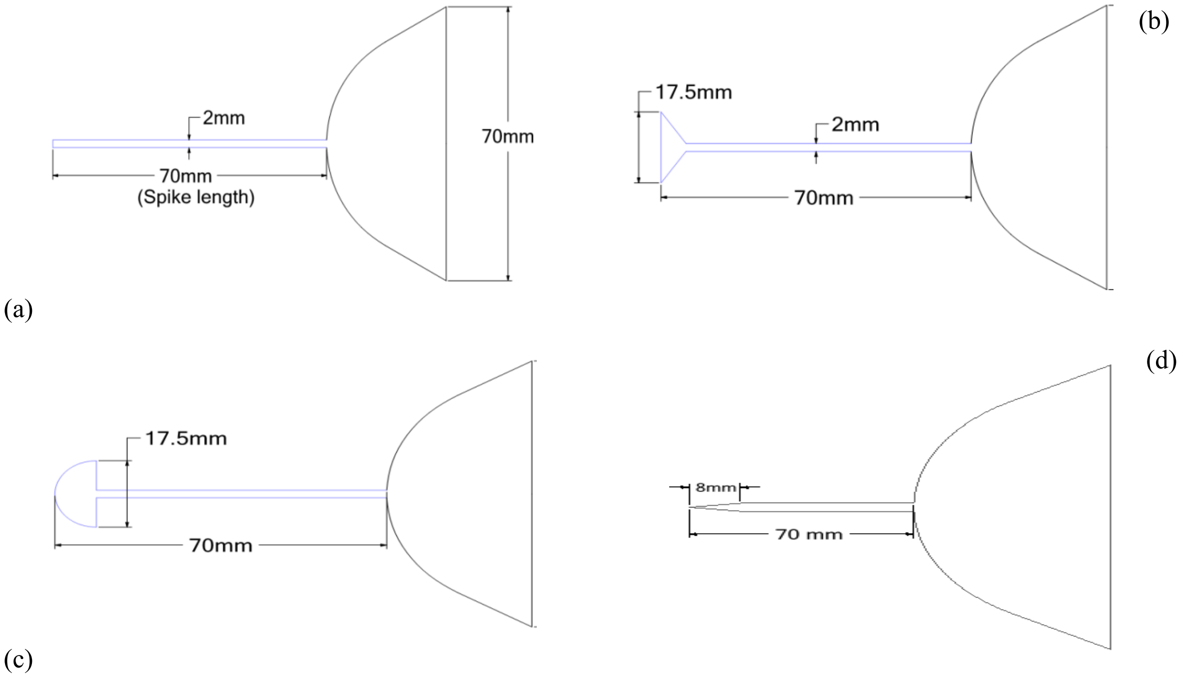

Fig.4 Diagrammatic representation of the 60-degree-apex-angle blunt cone equipped with a three kinds of aero-spikes (a) cut spike, (b) flat aero disk spike, (c) hemispherical disc spike, and (d) sharp spike 2D model respectively

3.2 Computational Grid

As mentioned, the current study employs a two-dimensional computational domain for the simulations. Previously, Gerdroodbary et al. have stated that 2D axisymmetric simulations are capable of accurately predicting the flow field and surface properties under similar flow conditions. (Gerdroodbary and Hosseinalipour 2010). Therefore, due to the symmetry of the body about its axis of rotation and the consideration of zero angle of attack of the flow, 2D-axisymmetric simulation is used instead of complete 3D simulation which reduced the computational time greatly. The domain is discretized using quadrilateral control volumes that do not overlap. Figure 5 provides a more detailed representation of the grid arrangement near the cut spiked nose cone. To meet the requirements of the two-equation turbulence model used in this study, a boundary layer meshing method is implemented near the wall region. The mesh has been appropriately set to capture the boundary layer and turbulent phenomena by choosing suitable values for the wall y-plus in order to account for the boundary layer and turbulence effects. To accurately capture turbulence and viscous effects, the grid is clustered near the wall.

This ensures that the y+ criterion is satisfied. It is important for the first grid cell to have a y+ value below 1 to properly resolve the viscous effects, as highlighted by John et al. (2021). The position of the first grid cell in each generated grid is determined based on the Mach number and running length of the case, ensuring that y+ < 1 is achieved according to the turbulent scaling. Figure 6 illustrates an example of the y+ variation over the cut spike under zero angle of attack conditions.

The grid resolution varies in the x-direction (along the body) between 200 and 500 grid points, and in the y-direction (perpendicular to the body) between 300 and 600 grid points. For the purpose of grid independence analysis, the total element count of the grid ranges from 61,800 to 298,000, ensuring reliable and accurate results. A separate grid test was conducted for mesh selection.

This variation in grid cell count ensures that the different geometries and configurations considered in the simulations are appropriately resolved, leading to accurate results.

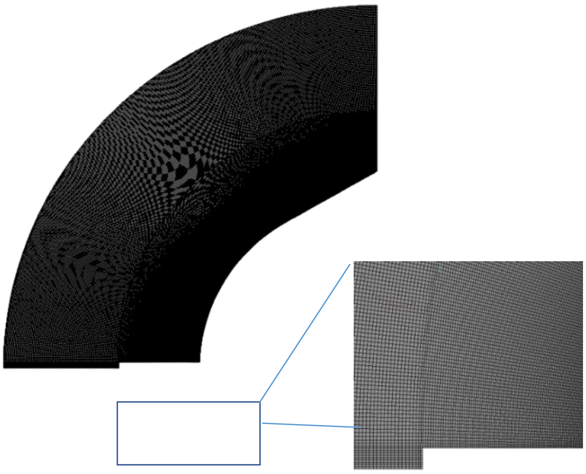

Fig. 5 Computational Grid

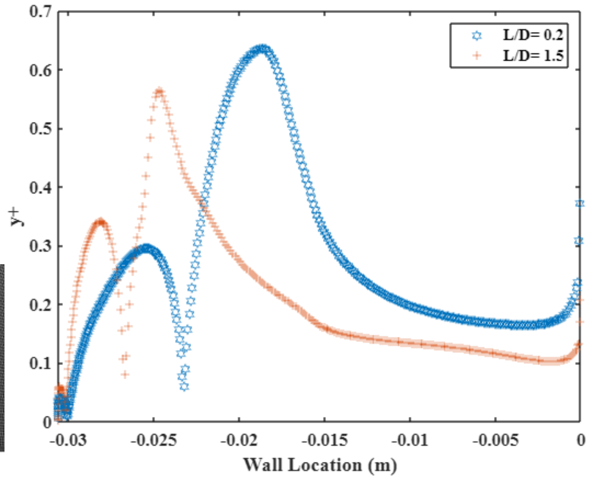

Fig.6 Wall y+ value over blunt surface

3.3 Boundary Condition

Figure 7 depicts the boundary conditions employed in the simulation of the computational domain. The specific boundary conditions utilized are as follows, Inlet: At the inlet of the computational domain, the flow's Mach 8.0, static pressure, and static temperature are prescribed. In this simulation, a hypersonic inlet is utilized with the following values: U_∞ = 2105.0 m/s, Reynold number $(R_e) = 5.5992 \times 10^5$ based on base diameter, Pressure P_∞ = 219.2 Pa and Temperature T_∞ = 172.4 K. Outlet: The variables at the outlet region are extrapolated from the interior domain. A pressure outlet condition is assigned to the nodes along the outlet boundary. Wall: The surfaces of the blunt cone and spike model are assumed to have a no-slip condition, and a wall boundary condition is applied. The walls are considered adiabatic. Symmetry/Axisymmetric: The remaining boundaries of the computational domain, excluding the inlet and outlet, are designated as symmetry planes. At these symmetry planes, the fluid velocity is tangential to the boundary.

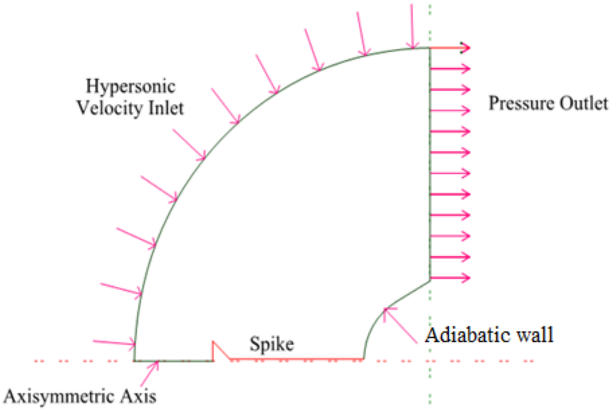

Fig.7 Boundary condition used for the simulations; Flat spike

Table 1 Free stream conditions air as free stream gas

Parameter	Value	Unit
T_∞	172.4	K
P_∞	219.2	Pa
U_∞	2105.0	m/s
M	8.0	--
ρ_∞	0.0044	Kg/m^3
T_{wall}	300	K
Reynold number (R_e)	5.5992×10^5	--

The flow conditions for the simulation can be found in Table 1, sourced from the reference by John et al. (2021). These boundary conditions significantly influence the flow behavior within the computational domain, ensuring accurate and reliable simulation results.

3.4 Solver Validation

When conducting numerical analysis through CFD codes, it is expected to validate outcomes by comparing them with existing analytical and experimental data. This process affirms the accuracy of your numerical analysis and ensures the production of reliable results. Two cases have been taken to validate the solver – the first involves estimating the shape of shock waves generated at high speeds, and the second involves calculating the drag value on the body. Initially, a validation investigation of this numerical study was carried out for the solver setup. The shape of the shock wave was compared with the correlation presented by Billig (1965) for Mach number 8 around a hemisphere. The hemisphere test model with a radius of 30 mm has been utilized for validation purposes. The correlations for the shock shape are drawn using Equation 1. The shock detachment distance was calculated using the standard correlation provided by Billig (1965), as given by Equation 2. The computed shock profile and stand-off distance in front of body in the absence of spike exhibit a strong agreement with the correlations proposed by Billig, as depicted in Figure 8.

As per equation (1), δ is shock stand-off distance which is obtained by using equation (2) and for Mach number 8.0. $R_c = 0.03613$, Is vertex radius of curvature and $\beta = 0.01253$, is shock angle in Equation (1).

$$x = R + \delta - R_c \cot^2 \beta \left[\left(1 + \frac{y^2 \tan^2 \beta}{R_c}\right)^{1/2} - 1\right] \text{ where, } \frac{R_c}{R} = 1.386\, exp\left(\frac{1.8}{(M_\infty - 1)^{0.75}}\right) \quad \frac{\delta}{R} = 0.143 e^{\left(\frac{3.24}{M_\infty^2}\right)} \qquad (1)$$

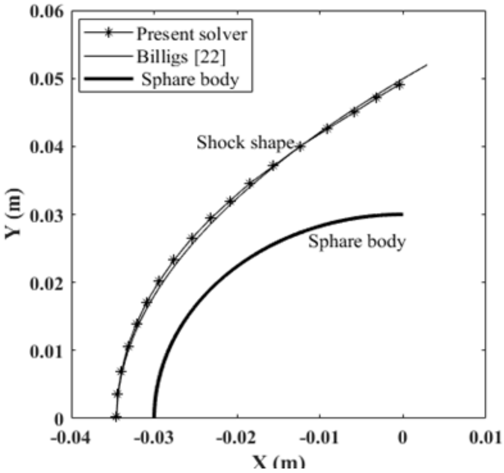

Fig. 8 Comparing the shape of shock waves using the Billig correlation with the solver

The computational solver yields a shock detachment distance of roughly 0.0045 meters, which closely corresponds to the observations derived from the empirical correlation depicted in figure 9. The results highlight that the deviation in δ remained below 4%.

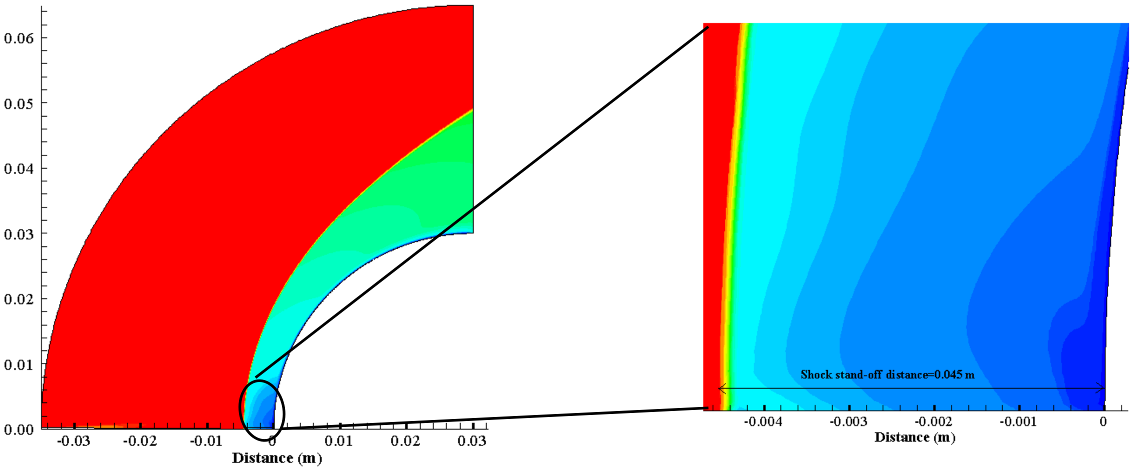

(Zoomed view)

Fig. 9 Shock stand-off distance (Present Solver)

Additionally, a contrast was drawn between the property relations acquired from the solver and the normal shock wave relation. Notably, it's crucial to acknowledge that the normal shock is situated at the blunt body's nose. This comparative analysis entailed consulting the research by various researcher, which furnishes the normal shock wave relation for γ=1.4. The outcomes of this juxtaposition have been succinctly presented in Table 2.

Table 2 Comparison of various parameters across shock (hemisphere)

Parameter	Normal shock wave theory	Present result	Deviation
P_{02}/P_1	74.50	74.72	0.2 %
T_2/T_1	13.38	13.41	0.2 %
ρ_{02}/ρ_{01}	5.56	5.53	0.5 %

These results demonstrate the capability of the current ANSYS CFD code to accurately handle high-speed flow conditions around the blunt body. Furthermore, for the purpose of validating the current numerical code, the scenario without a spike is employed as an initial benchmark for the computational framework of the ongoing study. In this validation study, the reference condition consists of a 60° blunt cone model in a hypersonic stream (Mach 8.0). The drag coefficient derived from the numerical simulation was 0.839, which closely aligns with the value of 0.844 determined by John et al. (2021) in their findings.

Table 3 Comparison of drag coefficient value with previous work

Parameter	Coefficient of drag		% error
Without spike	Present result	John et al. (2021)	
	0.839	0.844	0.5%

As depicted in Table 3, the drag coefficient derived from the numerical simulation was 0.839, exhibiting a notable similarity to the drag coefficient of 0.844 reported by John et al. (2021) in their numerical study.

3.5 Grid Independency Analysis

To ensure the solution's immunity to grid-dependent errors, a range of simulations were performed across various grid levels: coarse, medium, fine, and extra-fine. Details about the maximum grid element counts and y+ values for first cell near the wall for each level are outlined in Table 4. However, it's crucial to emphasize that this grid independence assessment is exclusively concentrated on the scenario without a spike. Importantly, the maximum y+ value of first cell near the wall remains below 1, confirming the accurate capture of turbulent phenomena. Furthermore, the grid close to the surface is appropriately concentrated to faithfully represent the underlying viscous effects.

Table 4 Grid independency study

Case	**Grid size**	**Element count**	**y+**
Coarse	200× 300	61,800	0.3281
Medium	250× 350	71,800	0.5421
Fine	360 × 450	1,60,200	0.8383
Extra-fine	500× 600	2,98,000	0.8379

Figure 10 illustrates the distribution of Cp (pressure coefficient) along the blunt wall. Notably, the absence of grid dependency is evident in the simulation when the element size is larger than 61,800. This analysis is conducted specifically on a 60-degree asymmetry cone at its apex angle. The numerical results affirm the calculations' grid independence. As a result, the medium grid scale is chosen for all cases, ensuring a balance between numerical accuracy and computational efficiency.

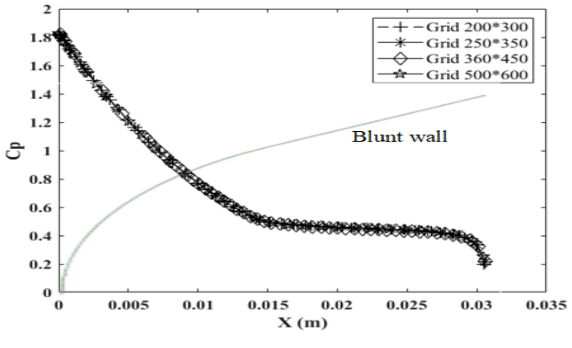

Fig.10 C_p plot for different grid used for grid independency study

3.6 Numerical Setup

The investigation concentrates on a two-dimensional axisymmetric compressible turbulent model, specifically assessing the steady-state flow patterns of the large-angle spiked blunt cone with an angle of attack (α) set at 0 degrees. The computational approach adopts a density-based formulation and employs a conservative finite volume control volume method for discretization. The fundamental governing equations taken into account comprise continuity, momentum, and energy equations, while presuming a two-dimensional axisymmetric flow. Consequently, the angular momentum equation remains unresolved. In order to determine the mean flow's five unknowns (namely pressure, u-velocity, v-velocity, temperature, and density), four governing equations are solved. For this study, the ideal gas equation of state is adopted, assuming the working medium (air) behaves as an ideal gas..

Convective fluxes at the boundaries of the computational domain are computed using the well-established upwind scheme (AUSM). Gradients at the cell centers are calculated using the cell-centered Green-Gauss approach. Fundamental gradients of flow properties are evaluated at the domain boundaries, and corresponding viscous fluxes are determined. In order to enhance solution accuracy, a spatial discretization approach with second-order precision is employed.

Rather than assuming a constant value, the viscosity is computed using Sutherland's law. A Prandtl number of Pr=0.71 is selected for the simulation. During the simulation, the time-step size can be adjusted by defining initial and final Courant-Friedrichs-Lewy (CFL) numbers. Initially, the time-step size is initialized at its maximum value, CFL=1. The convergence of two consecutive iterations at any grid point is determined by the convergence criterion for density: $|\rho^{n+1}$-$\rho^{n}| \leq 10^{-5}$, where 'n' signifies the iteration index.

The convergence plot, depicted in Figure 11, shows that the continuity residual stabilizes, maintaining an oscillatory state around the magnitude of 10^{-4}. To attain convergence, additional examination is undertaken concerning the time-dependent variation of the drag coefficient. During the progression of the flow field towards a steady state, the drag coefficient's variation tends to stabilize at a constant value, as demonstrated in Figure 12. Achieving convergence required approximately 4000 to 15000 iterations (time steps). The computational tasks were conducted on an Intel Core i5, 7th generation processor, operating at 2.75 GHz. The total duration of the simulation amounted to roughly 3 to 4 hours. The software execution was executed within a Windows 10 Professional operating environment.

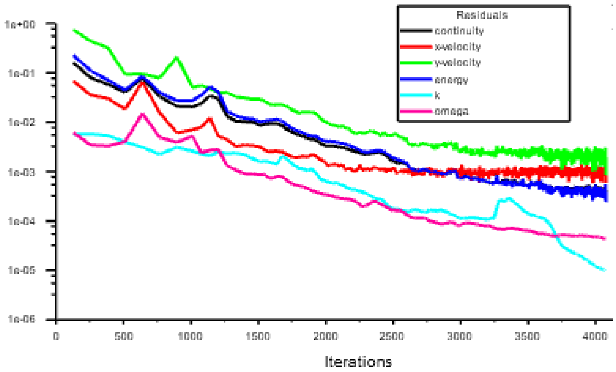

Fig. 11 Residual Plot

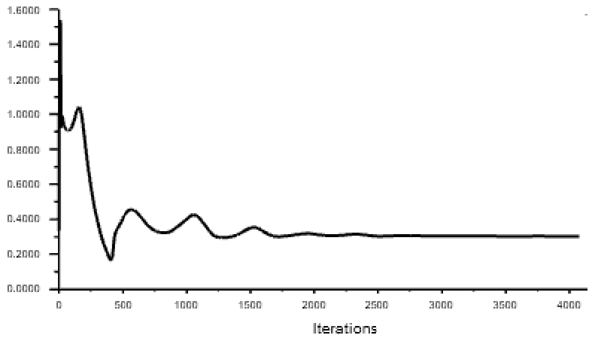

Fig. 12. Variation in Drag Coefficient

3.7 Governing Equations

The focus will be on solving the steady-state form of the governing equations, while also ensuring the stability of the chosen configuration. To close the equations, we will employ either the ideal gas equation of state or the perfect gas equation of state. Utilized a perfect gas model for simulations, noting its effectiveness primarily for low-enthalpy flows, as it maintains constant specific heats (Cp and Cv) and precludes any chemical reactions. The Reynolds-Averaged Navier-Stokes (RANS) equations constitute a system of partial differential equations employed in this simulation to characterize the averaged characteristics of turbulent fluid flow. ANSYS Fluent employs distinct governing equations tailored for numerical investigations, and these can be found in the official ANSYS Fluent documentation.

Continuity:

$$div.(\rho v) = 0 \tag{3}$$

Momentum:

$$div.(\rho vv) = -gradp + div.\mu\left[(gradv) - h\ \ \tfrac{2}{3} div.vI\right]$$
(4)

Energy:

$$div.(v(\rho E + p)) = div.(k_{eff} gradT\ \ + \left(\mu_{eff}\left[(gradv) - \tfrac{2}{3} div.vI\right].v\right)$$
(5)

Where, static pressure (p), density (ρ), air viscosity (μ), unit tensor (I), effective conductivity (k_{eff}), the total energy per unit volume (ρE), temperature (T). In Eq. (5), E = h – (p/ρ) + (1/2) $v^2 k_{eff}$ = kg+ kt, where kt = (Cpgμ_t)/ Pr_t, turbulent Prandtl number, (Pr_t) and μ_{eff} = μ + μ_t.

3.7.1 Turbulent Modeling

The Fluent CFD software allows users to choose from a range of turbulence models recognized for their reliable performance, efficiency, and reasonable accuracy in a wide array of turbulent flow scenarios. To effectively capture the turbulent characteristics of the flow field and estimate the mean flow parameters, supplementary equations are introduced in this study. The turbulence model adopted here is the k-ω SST Menter model (1994), which combines attributes from both the k-ε and k-ω models. Depending on the specific characteristics of the flow field, either the k-ω SST formulation or the k-ω model is activated. Specifically, the k-ω SST formulation is utilized in regions away from the boundary or wall, while the k-ω model is particularly effective in predicting flow separation and its timing under conditions of adverse pressure gradients. To facilitate the transition between these formulations, the concept of cross diffusion is applied. Consequently, our simulation approach involves employing the k-ω SST model, which is outlined as follows:

$$\frac{D(\rho k)}{Dt} = \tau_{ij}\frac{\partial u_i}{\partial x_j} - \beta \times \rho\omega k + \frac{\partial}{\partial x_j}\left[(\mu + \mu_k \mu_t)\frac{\partial k}{\partial x_j}\right]$$
(6)

$$\frac{D(\rho w)}{Dt} = \frac{Y}{v_t}\tau_{ij}\frac{\partial u_i}{\partial x_j} - \beta \times \rho\omega^2 + \frac{\partial}{\partial x_j}[(\mu + \mu_\omega \mu_t)\frac{\partial \omega}{\partial x_j} + \qquad 2\rho(1 - F_1)\sigma_{\omega^2}\frac{1}{\omega}\frac{\partial k}{\partial x_j}\frac{\partial \omega}{\partial x_j}$$
(7)

where, $F_1 = \tan h(\arg_1^4)$,

$$\arg_1^4 = \min\left(\max\left(\frac{\sqrt{k}}{0.09\omega y}; \frac{500v}{y^2\omega}\right); \frac{4\rho\sigma_{\omega 2}k}{CD_{k\omega}y^2}\right), \text{ and}$$

$$CD_{k\omega} = \max\left(2\rho\sigma_{\omega 2}\frac{1}{\omega}\right)\frac{\partial k}{\partial x_j}\frac{\partial \omega}{\partial x_j}, 10^{-20})$$

4. RESULT AND DISCUSSION

Numerical investigations were undertaken to examine the flow characteristics surrounding a blunt body, with and without attached spikes. The simulations were executed using the ANSYS Fluent software, encompassing both two-dimensional asymmetry and planar computations for both scenarios. Employing the methods previously delineated, the simulations generated numerical outcomes aimed at determining drag forces. These forces were assessed for three distinct spike shapes, each with varying length-to-diameter (L/D) ratios: 1.5, 1.0, 0.7, 0.5, and 0.2. The acquired results encompassed a spectrum of outcomes, effectively showcasing the impacts of spike length, table representation, and contour delineations. A comprehensive elaboration of these observations will be presented in the subsequent section.

4.1 Blunted cone without spike

Contour plots offer visual depictions of the simulated outcomes for the blunt cone model. The appearance of a pronounced bow shock in proximity to the body is responsible for generating substantial drag force, a phenomenon evident in Figure 13 through the static pressure contour. Furthermore, Figure 14 illustrates a substantial rise in temperature at the stagnation point. The elevated pressure and temperature in the nose region highlight the importance of mitigating these effects to curtail both wave drag and surface heat flux.

Figure 13 the contour representation of pressure distribution on the surface of the spike-less blunt body is illustrated in Figure 13, whereas Figure 14 presents the contour representation of temperature distribution. A prospective solution to tackle these issues involves the introduction of a retractable aero-spike flow modification method, conveniently applicable at the stagnation point of the blunt nose. Through numerical analysis, a drag coefficient value of 0.839 is obtained, closely corresponding with the observations made by John et al. (2021) this proposed technique demonstrates remarkable efficacy in mitigating wave drag and curtailing surface heat effects on the blunt body.

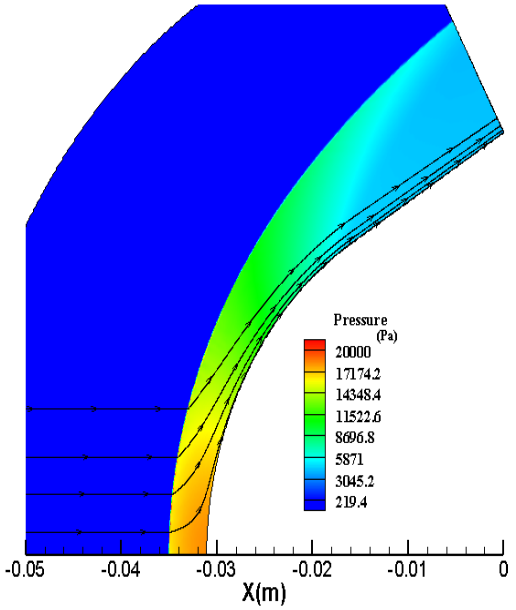

Fig. 13 Pressure contour over blunt body

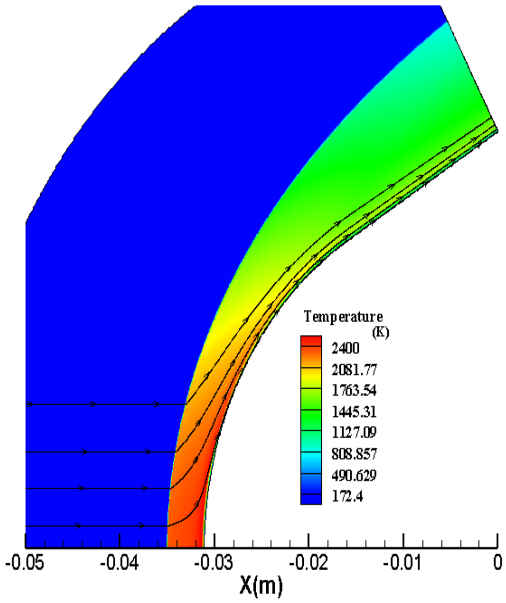

Fig. 14 Temperature contour over blunt body

4.2 Blunted cone with cut, flat, hemispherical and sharp spike

The drag coefficient values derived from numerical simulations for the blunt cone, considering various cut spike geometries and without are concisely summarized in Table 5 through Table 8. These simulations were executed at a zero-degree angle of attack, focusing on cut spikes with diverse Length to Base diameter (L/D) ratios: 1.5, 1.0, 0.7, 0.5, and 0.2. Some streamline visualizations of the flow fields encompassing the cut spike, flat spike, and hemispherical spike are presented in Figure 15, Figure 16, and Figure 17, respectively. These illustrations underscore the presence of a principal recirculation zone in the wake, generated due to favorable pressure gradients. Peripheral vortices are observed to exert minimal influence on the overall flow characteristics around the blunt cone.

Surface pressure distributions are scrutinized to examine the impact of various spike tip shapes and L/D ratios on shock layer reformation/modification and drag reduction. Figures 18 demonstrate that an increase in spike length corresponds to a reduction in surface pressure near the stagnation region for the cut spike, flat spike, and hemispherical spike, sharp respectively.

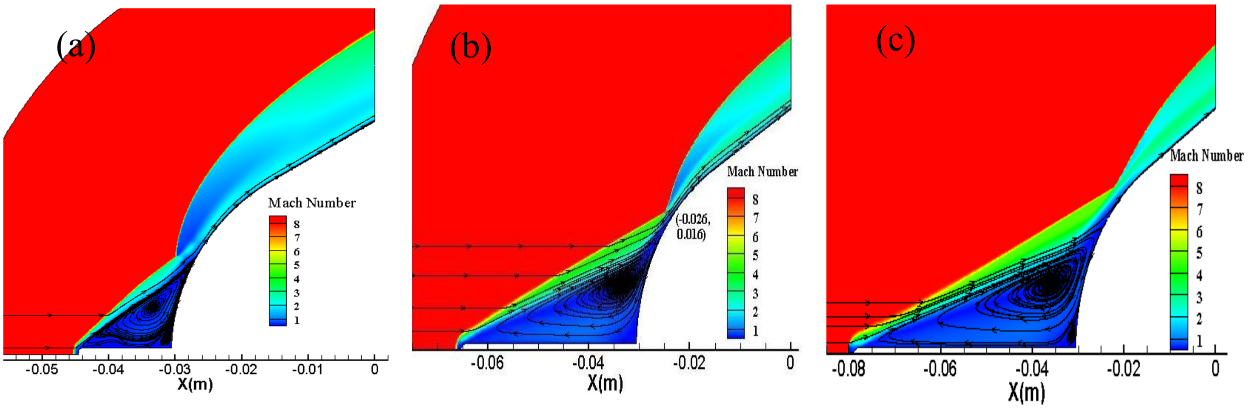

Fig.15 Computed flow field and Mach contour around the 60-degree blunt cone with a cut aerospike at an L/D of (a) 2.0 (b) 0.5 and (c) 0.7

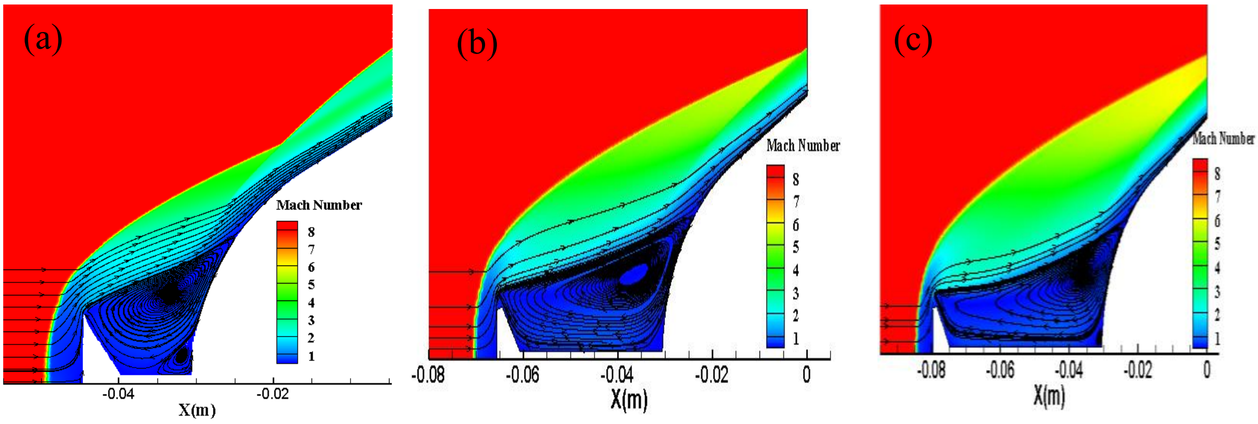

Fig.16 Computed flow field and Mach contour around the 60-degree blunt cone with a flat aerospike at an L/D of (a) 2.0 (b) 0.5 and (c) 0.7

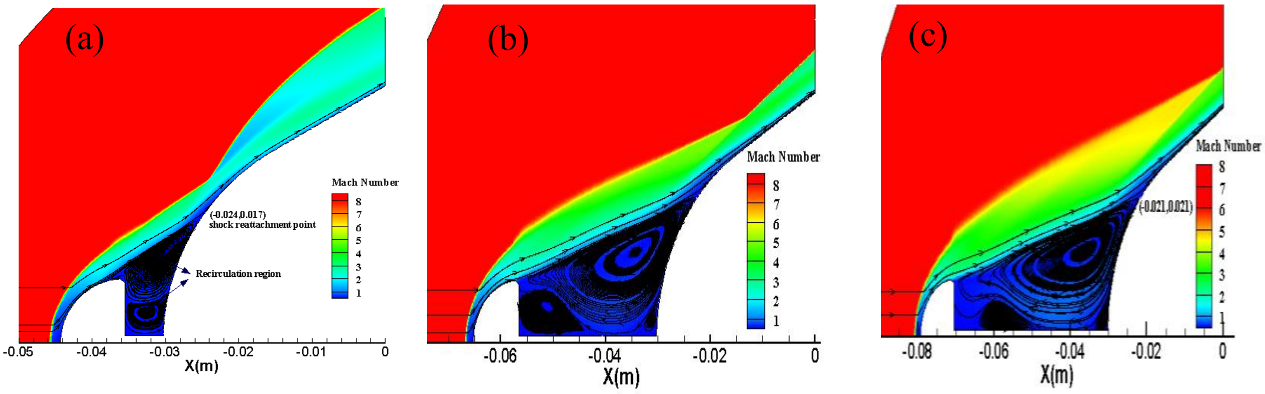

Fig.17 Computed flow field and Mach contour around the 60-degree blunt cone with a hemispherical aerospike at an L/D of (a) 2.0 (b) 0.5 and (c) 0.7

The contours of pressure and temperature underscore the role of the spike in curtailing both drag and surface temperature on the blunt surface. The sur face pressure ahead of the stagnation point is notably influenced by the recirculation region, and the point of reattachment, where the shock wave is re-compacted, is distinctly discernible through the pressure contour. A thorough analysis of wave drag reduction and flow field modification concerning spike length is presented in Table 5. These depictions portray the drag coefficient (Cd) variations for the sharp, cut, flat, and hemispherical aero-spikes, thereby highlighting the efficacy of differing spike configurations in mitigating drag.

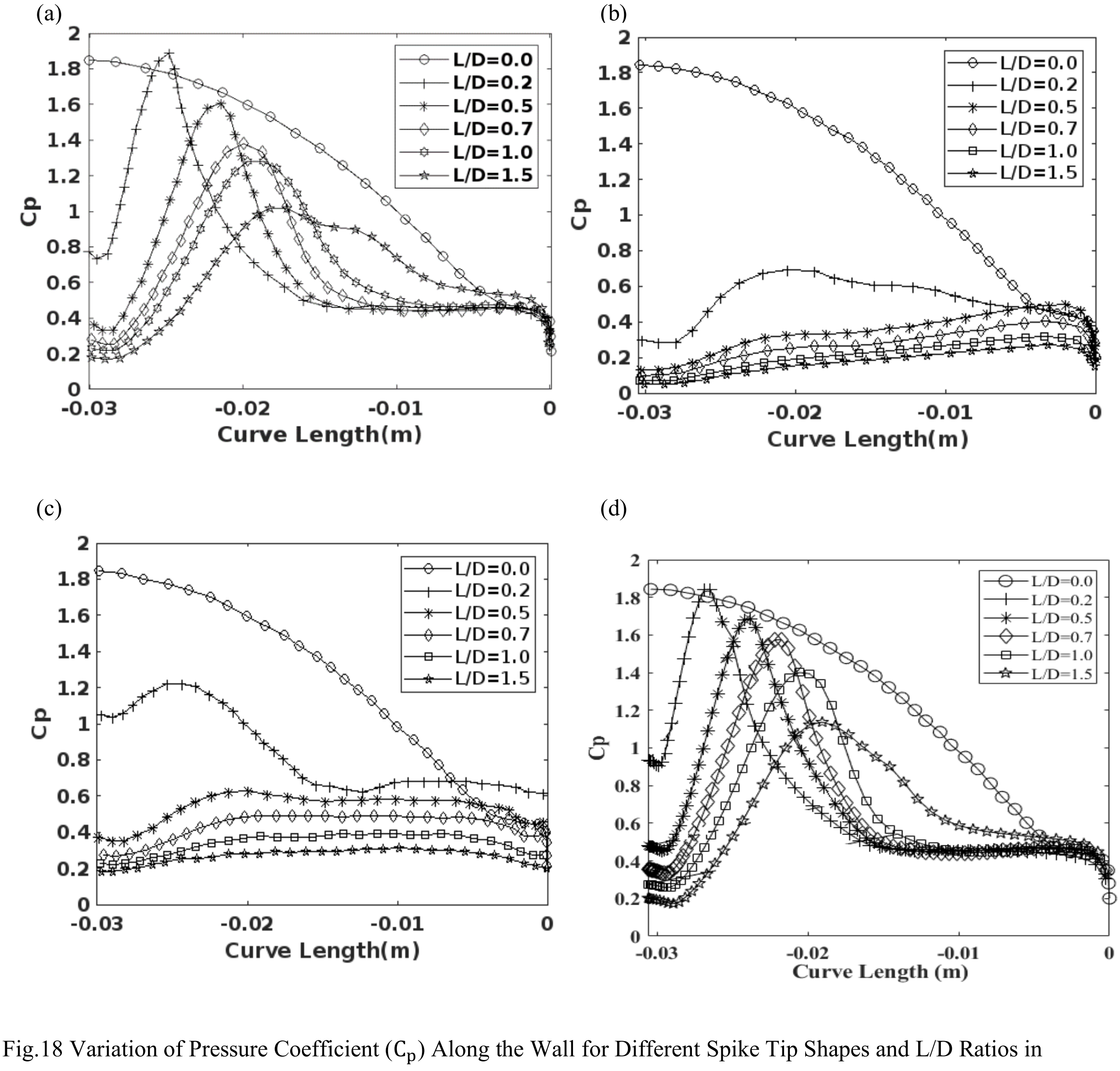

Fig.18 Variation of Pressure Coefficient (C_p) Along the Wall for Different Spike Tip Shapes and L/D Ratios in Hypersonic Flow Around a 60-Degree Blunt Cone: (a) Cut Spike, (b) Flat Spike, (c) Hemispherical Spike, (d) sharp spike

Table 5: Percentage Drag Reduction for Various L/D Ratios and Spike Tip Geometries in Hypersonic Flow Over a 60-Degree Blunt Cone: (a) Cut Spike, (b) Flat Spike, (c) Hemispherical Spike, (d) Sharp Spike

(a)

L/D ratio	$y+$	C_d	%Reduction (C_d)
Spike Less	0.1371	0.8383	---
0.2	0.2035	0.8207	2.1 %
0.5	0.1982	0.7261	13.4 %
0.7	0.2691	0.6756	19.4 %
1.0	0.8152	0.6654	20.6 %
1.5	1.1011	0.6281	25.1 %

(b)

L/D ratio	$y+$	C_d	%Reduction (C_d)
Spike Less	0.1371	0.8383	---
0.2	0.3295	0.5526	34.1 %
0.5	0.2161	0.3557	57.6 %
0.7	0.1393	0.2883	65.7 %
1.0	0.1545	0.2307	72.5 %
1.5	0.1948	0.1962	76.6 %

(c)

L/D ratio	$y+$	C_d	% Reduction (C_d)
Spike Less	0.1371	0.8383	---
0.2	0.2313	0.6411	23.6 %
0.5	0.3342	0.3237	61.38 %
0.7	0.1921	0.2534	69.77 %
1.0	0.9212	0.2001	76.14 %
1.5	0.7566	0.2479	79.11 %

(d)

L/D ratio	$y+$	C_d	% Reduction (C_d)
Spike Less	0.341	0.8383	---
0.2	0.234	0.8231	1.81 %
0.5	0.543	0.7702	8.12 %
0.7	0.342	0.7207	14.02 %
1.0	0.654	0.6788	19.02 %
1.5	0.452	0.6389	23.78 %

4.3 Using Short Spikes

In the present simulation, it's clear that using only the spike results in minimal drag reduction with a short sharp spike. Mounting a spike is a commonly employed method for decreasing drag force. However, to achieve significant drag reduction using a spike, an opposing-jet active technique can be employed simultaneously with the short spiked body.

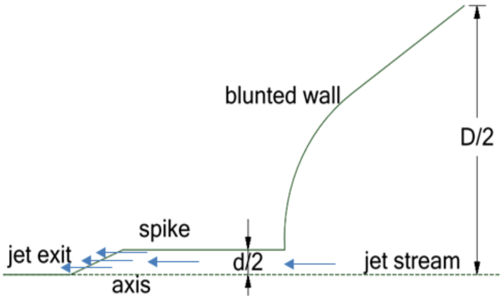

Fig. 19 Active opposing jet with sharp spiked body

Figure 19 depicts a schematic representation of the counter jet arrangement alongside the short sharp shaped spiked body. Air has been taken for the active method for injection gas. In a short spike with an L/D of 0.2, the least drag reduction is obtained. In a short spike with an L/D of 0.2, drag reduction can be increased using the active method. Injecting the jet at Mach 1, accompanied by a stagnation temperature of 300 K. Different total jet pressures of 4, 6, and 8 have been utilized to introduce the air jet from the tip of the spike. Pressure ratio is the ratio of stagnation pressure of the jet to the free stream stagnation pressure eq. (8).

$$\text{Pressure ratio (PR)} = P_{0j} / P_{0\infty} \tag{8}$$

An analysis for drag reduction by a short spike was conducted using three pressure ratios: 21.8, 32.8, and 43.7. To achieve this objective, Figure 20 displays the computed Mach contour. The initiation of the active opposing jet results in the expansion of the upstream flow at the tip of the spike.

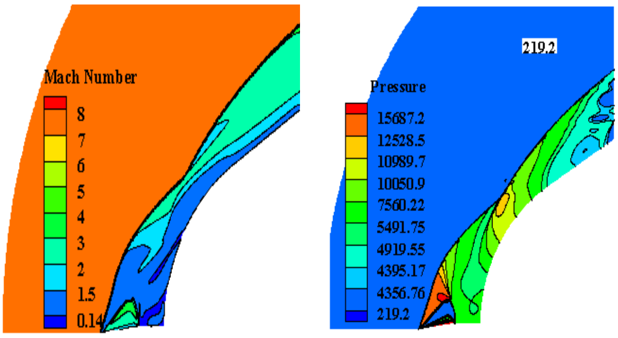

Fig. 20 depicts Mach and pressure contours for the active opposing jet case.

In these pressure ratios, drag reduction of approximately 61.15%, 76.02%, and 86.9% was observed, respectively. Incorporating the active method can lead to an enhancement in drag reduction, as evident from the analysis. It is feasible to attain significant drag reduction using a short spike.

5. CONCLUSION

This study involved conducting numerical simulations on a 60° apex angle blunt cone with a 70 mm base diameter and a bluntness ratio of 0.857, operating within a Mach 8 free stream. The primary aim was to explore the wave drag reduction achievable by employing various lengths and shapes of forward-facing spikes, relative to an un-spiked nose cone. The investigation focused on assessing the aerodynamic impacts of mechanical spikes on wave drag reduction at hypersonic velocities. The key findings are summarized as follows:

(1) At zero angles of attack, the sharp spike exhibited the least drag reduction, ranging from a maximum of 23.78% for a 105 mm spike length to a minimum of 1.81% for a 14 mm spike length. The sharp spike configuration yielded a smaller shock angle compared to the blunt, cut, flat, and hemispherical spikes.

(2) The cut-shaped spike exhibited a marginal improvement over the sharp spike in terms of drag reduction. For cut spikes, drag reduction ranged from approximately 2.1% (14 mm spike length) to about 25.1% (105 mm spike length).

(3) The flat aero-disk, featuring an L/D ratio of 1.5 mounted on the nose cone, displayed substantial drag reduction, ranging from 34.1% to an impressive 76.6%. Notably, across all spike tip shapes, an increase in spike length corresponded to a significant rise in drag reduction.

(4) Among the spike configurations, the hemispherical spike showcased the highest drag reduction at zero angles of attack, ranging from a maximum of 79.11% (105 mm spike length) to a minimum of 23.6% (14 mm spike length).

(5) There is potential to reduce more drag even with a short spike if the active opposing jet method is employed alongside the spike. A notable decrease in drag, approximately 86.9%, was achieved by combining a short spike with a counter jet at a pressure ratio of 43.7.

Collectively, these findings underscore the effectiveness of mechanical spikes in mitigating drag under hypersonic flow conditions. In conclusion, this study offers valuable insights into the aerodynamic behaviour of diverse spike configurations, highlighting their potential for reducing wave drag and surface heat flux in hypersonic flow environments.

REFERENCES

1. Snezana, M., & Pavlovic, M. D. (2005). Influence of Spike Shape at Supersonic Flow past Blunt-Nosed Bodies: Experimental Study. AIAA Journal, 40(5), 1018-1020. https://doi.org/10.2514/2.1745
2. Tahani, M., Karimi, M. S., Mahmoudi, M., & Mirmahdian, S. (2013). Numerical investigation of drag and heat reduction in hypersonic spiked blunt bodies. Journal of Heat and Mass Transfer, 49(10), 1369–1382. DOI:10.1007/s00231-013-1173-4
3. Kamyar, M., & Khorsandi, M. (2014). The drag reduction in spherical spiked blunt body. Acta Astronautica, 99, 92-98. https://doi.org/10.1016/j.actaastro.2014.02.009
4. Crawford, D. H. (1959). Investigations of the flow over a spiked-nose hemisphere cylinder. NASA TN D-118. https://catalog.hathitrust.org/Record/011447845
5. Wood, C. (1962). Hypersonic flow over spiked cones. Journal of Fluid Mechanics, 12. https://doi.org/10.1017/S0022112062000427
6. Ahmed, M., & Qin, N. (2011). Recent advances in the aerothermodynamics of spiked hypersonic vehicles. Progress in Aerospace Sciences, 47, 425-449. DOI:10.1016/j.paerosci.2011.06.001
7. Bogdonoff, S., & Vas, I. (1959). Preliminary Investigations of Spiked Bodies at Hypersonic Speeds. Journal of the Aerospace Sciences, 26, 65-74. DOI:10.1017/S0001924000002554
8. Mehta, R. (2012). Numerical heat transfer study around a spiked blunt-nose body at Mach 6. Heat and Mass Transfer, 49, 485-496. DOI:10.1007/s00231-012-1095-6
9. Huang, J., Li, P., & Yao, W. (2018). Thermal protection system gap analysis using a loosely coupled fluid-structural thermal numerical method. Acta Astronautica, 146, 368-377. https://doi.org/10.1016/j.actaastro.2018.02.047
10. Kharati-Koopaee, M., & Gazor, H. (2017). Assessment of the Aerodisk Size on Drag Reduction and Thermal Protection of High-Bluntness Vehicles at Hypersonic Speeds. Journal of Aerospace Engineering, 30. https://doi.org/10.1061/(ASCE)AS.1943-5525.000070
11. Gauer, M., & Paull, A. (2008). Numerical Investigation of a Spiked Blunt Nose Cone at Hypersonic Speeds. Journal of Spacecraft and Rockets, 45, 459-471. https://doi.org/10.2514/1.30590
12. Gerdroodbary, M., & Hosseinalipour, S. (2010). Numerical simulation of hypersonic flow over highly blunted cones with spike. Acta Astronautica, 67, 180-193. https://doi.org/10.1016/j.actaastro.2010.01.026
13. Myshenkov, V. (1982). Numerical investigation of separated flow in front of a spiked cylinder. Fluid Dynamics, 16, 938-942. https://doi.org/10.1007/BF01089728
14. Paskonov, V., & Cheraneva, N. (1984). Numerical investigation of laminar separation in the case of supersonic flow of viscous gas past spiked bodies. Fluid Dynamics, 19, 281-285. https://doi.org/10.1007/BF01091252
15. Patil, A., Kumar, S., & Kulkarni, V. (2022). Analysis of counter flow injection technique at elevated enthalpy hypersonic reacting flows. International Journal of Heat and Mass Transfer, 182, 121893. https://doi.org/10.1016/j.ijheatmasstransfer.2021.121893
16. Kumar, S., & Kulkarni, V. (2020). Drag of a Spiked Body in Chemically Reacting Hypersonic Flow. Journal of Spacecraft and Rockets, 57, 1092-1097. https://doi.org/10.2514/1.A34764

17. Kulkarni, V., & Reddy, K. (2008). Enhancement in counterflow drag reduction by supersonic jet in high enthalpy flows. Physics of Fluids, 20, 016103. https://doi.org/10.1063/1.2813042
18. John, B., Bhargava, D., Punia, S., & Rastogi, P. (2021). Drag and Heat Flux Reduction using Counterflow Jet and Spike - Analysis of their Equivalence for a Blunt Cone Geometry at Mach 8. Journal of Applied Fluid Mechanics, 4(2), 375-388. DOI:10.47176/JAFM.14.02.31648
19. Venukumar, B., & Reddy, K. P. J. (2007). Experimental investigation of drag reduction by forward facing high-speed gas jet for a large angle blunt cone at Mach 8. Saadhana Journal, 32(1&2), 123–131. DOI:10.1007/s12046-007-0011-0
20. Venukumar, B., Jagadeesh, G., & Reddy, K. (2006). Counterflow drag reduction by supersonic jet for a blunt body in hypersonic flow. Physics of Fluids, 18, 118104. https://doi.org/10.1063/1.2401623
21. Menezes, V., Saravanan, S., Jagadeesh, G., & Reddy, K. (2003). Experimental Investigations of Hypersonic Flow over Highly Blunted Cones with Aerospikes. AIAA Journal, 41, 1955-1966. https://doi.org/10.2514/2.1885
22. Billig, F. (1967). Shock-wave shapes around spherical-and cylindrical-nosed bodies. Journal of Spacecraft and Rockets, 4, 822-823. https://doi.org/10.2514/3.28969
23. John, A. Jr. (1989). Hypersonic and High Temperature Gas Dynamics. McGraw-Hill, US.
24. Menter, F. (1994). Two-equation eddy-viscosity turbulence models for engineering applications. AIAA Journal, 32, 1598-1605. https://doi.org/10.2514/3.12149
25. Lee, H. J., Lee, B. J., Kim, S. D., & Jeung, I. (2011). Flow characteristics of smallsized supersonic inlets. J. Propul. Power, 27(2) 306-318. https://doi.org/10.2514/1.46101.